Crystallization and Electron Paramagnetic Resonance Characterization of the Complex of Photosystem I with its Natural Electron Acceptor Ferredoxin

Petra Fromme,*† Hervé Bottin,‡ Norbert Krauss,§ and Pierre Sétif‡

*Max Volmer Laboratorium, Institut für Chemie, Fakultät II, Technische Universität Berlin, 10623 Berlin, Germany; †Department of Chemistry and Biochemistry, Arizona State University, Tempe, Arizona 85287-1604 USA; ‡Département de Biologie Joliot Curie, Commissariat à l'Energie Atomique, Service de Bioénergétique and CNRS URA 2096, Gif sur Yvette 91191, France; and §Institut für Chemie/Kristallographie, Freie Universität Berlin, D-14195 Berlin, Germany

ABSTRACT The formation of a transient complex between photosystem I and ferredoxin is involved in the process of ferredoxin photoreduction in oxygenic photosynthetic organisms. Reduced ferredoxin is an essential redox intermediate involved in many assimilatory processes and is necessary for the reduction of $NADP^+$ to NADPH. Single crystals from a complex of photosystem I with ferredoxin were grown using PEG 400 and $CaCl_2$ as precipitation agents. The crystals diffract x-rays to a resolution of 7–8 Å. The space group was determined to be orthorhombic with the unit cell dimensions $a = 194$ Å, $b = 208$ Å, and $c = 354$ Å. The crystals contain photosystem I and ferredoxin in a 1:1 ratio. Electron paramagnetic resonance (EPR) measurements on these crystals are reported, where EPR signals of the three [4Fe-4S] clusters F_A, F_B, F_X, and the [2Fe-2S] cluster of ferredoxin were detected. From the EPR spectra observed at three particular orientations of the crystal in the magnetic field, the full orientation pattern of the F_A^- g-tensor was simulated. This simulation is consistent with the presence of 12 magnetically inequivalent F_A^- clusters per unit cell with the C_3 axis of the PSI trimers oriented at (23°, 72°, 77°) to the unit cell axes.

INTRODUCTION

In oxygenic photosynthetic organisms, photosystem I (PSI) catalyzes the light-driven electron transport between soluble electron carriers, from cytochrome c_6 at the lumenal side to ferredoxin at the stromal (cytoplasmic) side of the thylakoid membrane. In case of iron deficiency, flavodoxin can also act as a soluble electron carrier at the acceptor side of PSI (Rogers, 1987). Ferredoxin functions as the soluble electron donor to ferredoxin-$NADP^+$ reductase (FNR), which catalyzes the reduction of $NADP^+$ to NADPH in chloroplasts and cyanobacteria. Furthermore, ferredoxin is involved in the assimilation of nitrogen and sulfur and in the regulation of carbon assimilation (Knaff, 1996). Therefore, the complex of PSI with ferredoxin can be regarded as a model system for the interaction of electron transfer proteins.

Very recently, the structure of PSI was solved at 2.5 Å resolution (Jordan et al., 2001). From this structure, previous evidence that all of the three membrane extrinsic subunits PsaC, PsaD, and PsaE are involved in the interaction of PSI with ferredoxin was strongly supported. Modeling of the interaction of ferredoxin from *Spirulina platensis* (Tsukihara et al., 1981) to the 6 Å electron density map of PSI from *Synechococcus elongatus* (Krauss et al., 1993) led to the suggestion of a binding site of ferredoxin, which is located close to the terminal 4Fe-4S cluster of PSI (Fromme et al., 1994). The distance between the 4Fe-4S cluster of PSI to the 2Fe-2S cluster of ferredoxin was estimated to be ≈14 Å (center-to-center distance). This would lead to an edge-to-edge distance of 11–12 Å. This distance is in reasonable agreement with the fastest kinetics of the electron transport from PSI to ferredoxin, which was determined to exhibit a halftime of 500 ns (Sétif and Bottin, 1994, 1995). The same binding site was found by electron microscopy of cross-linked complexes of PSI with either ferredoxin (Lelong et al., 1996) or flavodoxin (Mühlenhoff et al., 1996). At this binding pocket, ferredoxin would get in contact with all three stromal subunits, which is in good agreement with the functional studies (reviewed in Sétif, 2001).

Nevertheless, information concerning the docking site at the atomic level, including the orientation of ferredoxin and the identification of the specific interactions between the partners, is still missing. To get further knowledge in the interaction of ferredoxin with PSI, we started experiments on the cocrystallization of these two proteins. In this report we describe the preliminary characterization of the PSI/ferredoxin cocrystal and provide evidence for a functional 1:1 PSI/ferredoxin complex in the cocrystals. Moreover, the EPR characterization of the F_A^- g-tensor in the cocrystals was performed and was used for deducing the orientation of the C_3 axis of the trimer relative to the unit cell axes. This information was used for deriving the characteristics of the F_B^- g-tensor.

Submitted March 26, 2002, and accepted for publication June 13, 2002.

Address reprint requests to Pierre Sétif, CE Saclay Bâtiment 532 DBJC/SBE, Gif sur Yvette 91191, France. Tel.: 33-1-69089867; Fax: 33-1-69088717; E-mail: setif@dsvidf.cea.fr.

Norbert Krauss's present address is Institut für Biochemie, Universitätsklinikum Charite, Medizinische, Fakultät der Humboldt Universität zu Berlin, Monbijoustrasse 2, D-10117 Berlin, Germany.

0006-3495/02/10/1760/14 $2.00

MATERIALS AND METHODS

Isolation of PSI and ferredoxin

PSI from the thermophilic cyanobacterium *S. elongatus* was isolated in the presence of the stereochemically pure detergent β-dodecylmaltoside as

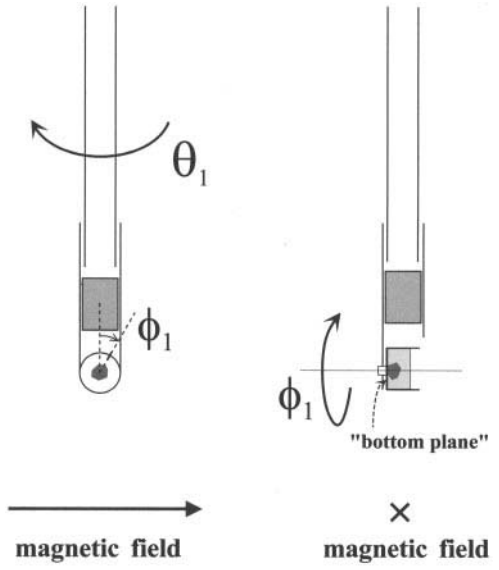

FIGURE 1 Scheme of the crystal holder used for changing the orientation of the cocrystals in two orthogonal directions. The θ_1 angle was changed with a goniometer by steps of 5° and the ϕ_1 angle was adjusted manually, with a precision of ~5°, under a binocular microscope (20× magnification) while the crystal holder was maintained above a bath of liquid nitrogen. The holder was made of Plexiglas and its upper part was adapted to a standard quartz EPR tube.

described elsewhere (Fromme and Witt, 1998). Ferredoxin used in this study was isolated from the cyanobacterium *Synechocystis* sp. PCC 6803 as described in Bottin and Lagoutte (1992). The rates of photoreduction and the properties of PSI binding of this ferredoxin were found to be very similar for PSI from either *S. elongatus* or *Synechocystis* 6803 (Sétif and Bottin, 1994).

Preparation of cocrystals for EPR measurements

For single-crystal studies, a cocrystal within a drop of PEG buffer (43% PEG (w/v) in 100 mM HEPES pH 7.5, 150 mM $CaCl_2$, 0.02% β-DM) was gently deposited onto the holder surface (bottom plane of Fig. 1). The PEG 400 concentration was increased from 14% (concentration in the crystallization buffer) up to 43%, to ensure a conservation of the cocrystals during the freezing process needed for performing low temperature EPR. This was done in several steps by increasing the PEG amount by 4% increments with a 5 min incubation at each intermediate PEG concentration. The cocrystals were kept for at least 10 min at room temperature with the final 43% PEG concentration before freezing. Different samples were prepared at various pH values (between 6.0 and 9.2) and with different reductants (sodium ascorbate or dithionite) and redox mediators (2,6-dichlorophenol-indophenol (DCPIP), phenazine methosulfate (PMS), methyl viologen), which were added at the final stage (43% PEG). Incubation in dim room light or in darkness was performed for times as long as several hours. For freezing, cocrystals were dipped into liquid nitrogen. There was no apparent degradation of the cocrystals during these treatments. Incubation of cocrystals at 200 K was performed outside the EPR cavity in a nitrogen gas flow system (BVT-3000 from Bruker, Wissembourg, France). A detailed EPR investigation was performed for two different cocrystals, which were treated as follows: for the first one, designated **1**, 10 mM sodium ascorbate and 0.5 mM DCPIP were added to the final solution (43% PEG, pH 7.5). The cocrystal was then incubated in darkness for 10 min before freezing under dim room light; for the second one, **2**, 10 mM sodium dithionite and 0.5 mM PMS were added to the final solution (43% PEG, pH 6.5). The cocrystal was then incubated in darkness for 8 min in a vessel filled with argon gas before freezing in darkness.

The unit cell axes were difficult to correlate to the morphological shape of the EPR-studied large cocrystals. The crystals displayed many facets and did not exhibit either an edge or a face that was significantly larger than the others, so they were first placed randomly in the special holder. After mounting, the holder was rotated by 180° in 5° steps and EPR spectra were recorded to find an orientation where the crystal could be rotated around one of the crystallographic axes.

Powder-spectra of cocrystals were obtained using a large number (>50) of small and randomly oriented cocrystals. Samples were prepared in the crystallization medium (150 mM $CaCl_2$, 14% PEG 400, 0.02% β-DM) with addition of redox mediators. Incubation was performed at room temperature in dim room light under argon flow. Cocrystals were then rapidly sedimented by a brief centrifugation (1 min) in a small quartz tube and frozen by dipping into liquid nitrogen.

EPR measurements

EPR spectra were recorded between 10 and 45 K with an ESR300D X-band spectrometer (Bruker), using a TE_{102} resonator equipped with a front grid for sample illumination within the cavity. Samples were illuminated within the cavity using a tungsten-halogen lamp (800 W). White light was filtered with an infrared filter (Calflex) and a water cuvette. Light was focused onto the cavity grid by a Plexiglas lightpipe. The temperature was controlled with an ESR9 helium cryostat (Oxford Instruments, Oxon, UK). Illumination outside the EPR cavity was performed at 200–240 K in a nitrogen gas flow system (BVT-3000 from Bruker) and the same lamp as above as the light source. For spin quantitation, double integration of the spectra was performed after subtraction of the radical signal in the $g_{\text{free electron}}$ region, when present. In the case of a light-induced spectrum relative to a single orientation of a single cocrystal, the quasi-isotropic radical signal from $P700^+$ was subtracted after measuring it from the average spectrum of a whole series of θ_1 angles (from 0 to 175°).

The following procedure was used for estimating the PSI/ferredoxin stoichiometry in the cocrystals: after its EPR study, an EPR sample containing many small cocrystals was dissolved. Part of the sample was studied by flash-absorption spectroscopy. Measurements were performed at 820 nm, from which the $P700^+$ concentration (=[PSI]) was estimated, assuming an absorption coefficient of 6500 M^{-1} cm^{-1} (Mathis and Sétif, 1981). Another part of the sample was used for preparing an EPR tube under conditions (pH 9.0 + dithionite), which allowed ferredoxin to be fully reduced. This was compared to a reference sample containing a known amount of ferredoxin from *Synechocystis* 6803. This amount was calculated by assuming an absorption coefficient of 9500 M^{-1} cm^{-1} for oxidized ferredoxin at 423 nm (Tagawa and Arnon, 1968; Fee and Palmer, 1971). The ferredoxin sample was reduced with an excess of sodium dithionite at pH 8.7. For a quantitative EPR comparison of the ferredoxin contents of the samples, spectra were recorded at 45 K under conditions of nonsaturating microwave power. At this temperature, the ferredoxin signal could be observed in the PSI/ferredoxin sample with little interference from F_A^- and F_B^- as the EPR spectra of these last species are severely broadened due to fast spin-lattice relaxation (see Lelong et al., 1994) for a similar quantitation).

For measurements on single cocrystals, the crystal holders were made of Plexiglas (Atecplast, Bezons, France). Their orientation could be changed in two orthogonal directions (Fig. 1): the θ_1 angle was changed with a goniometer by 5° steps from 0 to 180°. For measuring light-induced spectra, a series of baselines was recorded before illumination by varying the θ_1 angle and spectra after illumination were recorded later on at the same angles. The angle ϕ_1 was changed manually, with a precision of ~5°, under a binocular microscope (20× magnification) while the crystal holder was maintained above a bath of liquid nitrogen. Complete sets of data were recorded for two different cocrystals, but data for only one of these will be

shown in the present report. For both cocrystals, P700 was initially reduced and the iron-sulfur centers were initially oxidized before freezing in darkness, as checked by the almost absence of EPR signal before illumination (only a very weak radical was observable). An EPR baseline was then recorded in darkness at 10–20 K at different θ_1 orientations before 10 min illumination within the cavity. Illumination was performed while rotating the sample holder for improving the homogeneity of illumination. A longer period of illumination did not increase the size of the light-induced spectra, thus indicating that all PSIs in the cocrystals were photoexcited during the 10-min period. EPR spectra were then recorded at the different θ_1 orientations and light-induced spectra were obtained after subtraction of the baseline. A dataset was thus recorded by varying θ_1 with the goniometer from 0 to 180° by 5° steps. Similar datasets were recorded at different ϕ_1 angles to get a complete orientation pattern. For doing this, it was necessary to incubate the crystals between two consecutive datasets at 200 K in darkness for periods of ~30 min, which resulted in a complete recombination between $P700^+$ and $(F_A, F_B)^-$, as checked by EPR. The temperature of a cocrystal was therefore changed many times between 10 and 20 K, 77 K (for intermediate storage), and 200 K without any observable induced damage as checked by the absence of change in the light-induced EPR spectrum at a given orientation. It appears therefore that the PSI/ferredoxin cocrystals are much more resistant than the PSI crystals (further named PSI_a for PSI-alone crystals to discriminate them from the PSI/ferredoxin cocrystals). This allows various redox reagents and light treatments to be used for getting a variety of redox states that may be useful for future studies by x-ray crystallography and EPR at low temperature.

EPR simulations were performed using Mathcad (V. 8.0, Mathsoft, Inc., Cambridge, MA). The systematic parameter search was performed using Borland Pascal programs for Windows (V. 7.0, Borland International, Inc., Scotts Valley, CA). All programs were home-written. Fitting with Gaussian components was performed with the software Origin (V. 6.0, Microcal Software, Inc., Northampton, MA).

RESULTS

Crystallization of the PSI/ferredoxin complex

A large screening of different crystallization conditions was used for testing the stability and the solubility of the intact PSI/ferredoxin complex. In the following, we describe the main parameters that influence the solubility of the complex.

Ionic strength

One expects an increase in the ratio of hydrophilic to hydrophobic surface areas by the docking of ferredoxin to the PSI complex, leading to an increase of the complex solubility as a whole. This leads to a high solubility of the PSI/ferredoxin complex compared to PSI_a without ferredoxin, which was crystallized successfully by dialysis against low ionic strength (Fromme and Witt, 1998). The PSI/ferredoxin complex is soluble up to concentrations of 150 mg/ml in buffer without salt (5 mM MES-Na, pH 6.4, 0.02% β-DM). Single crystals of PSI can even be dissolved by addition of ferredoxin. Therefore, the PSI/ferredoxin-complex could not be crystallized by "reverse of salting in" like PSI_a.

Crystallization agents

The cocrystallization of PSI of *S. elongatus* with ferredoxin from *Synechocystis* 6803 was achieved by the use of the crystallization agent polyethyleneglycol (PEG 400) in the presence of $CaCl_2$, using vapor diffusion techniques. The best cocrystals were grown at medium ionic strength (0.45). We found Cl^- ions to be essential for the crystallization. There was no evidence for anion specificity. Monovalent (Na^+/NH_4^+) and divalent cations (Mg^{2+}/Ca^{2+}) could be used. The best crystals were grown in the presence of $CaCl_2$. Fig. 2 *A* shows a picture of the cocrystals (see figure legend for exact crystallization conditions). The morphology of the cocrystals is different from the hexagonal crystals of PSI (Fromme, 1996; Fromme and Witt, 1998). The new crystal form is induced by ferredoxin. Small hexagonal needles are observed if the pure PSI complex is used for crystallization experiments under the same conditions.

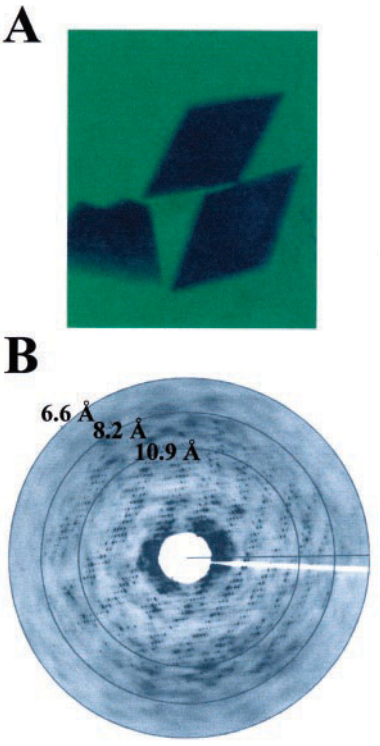

FIGURE 2 Cocrystals of photosystem I with ferredoxin and diffraction pattern. (*A*) Picture of the PSI/ferredoxin cocrystals. The crystals were grown by vapor diffusion: protein-solution (3 μl): 100 μM PSI (P700), 125 μM ferredoxin, 22 mM HEPES, pH 7.5, 50 mM $CaCl_2$, 0.013% β-dodecylmaltoside, 4.7% PEG 400; reservoir (900 μl): 0.1 M HEPES pH 7.5, 0.15 M $CaCl_2$, 0.013% β-dodecylmaltoside, 14% PEG 400. The crystals shown herein have a size of 0.3 mm. (*B*) Diffraction pattern of photosystem I/cocrystals obtained at beamline ID14–1 at ESRF in Grenoble; wavelength 1 Å. The resolution is indicated by the circles.

pH dependence

The solubility of the PSI/ferredoxin complex was investigated in the pH range from 5.5 to 9.5, with only a small increase in solubility with pH. Cocrystals of the same morphology were grown at the fully tested pH range. The cocrystals are stable over this pH range. This was a major

achievement, compared to the PSI_a crystals, because it opens the way to the controlled prereduction of some of the FeS clusters in one single crystal with reductants with a pH-dependent effective E_m such as dithionite.

Temperature dependence

The temperature dependence of the cocrystallization differs from the one observed during the crystallization of PSI_a at low ionic strength, where the optimum temperature for crystal growth was determined to be 4°C (Fromme and Witt, 1998). The PSI/ferredoxin complex was grown in the presence of $CaCl_2$ and the crystallization agent PEG 400. In the presence of PEG, a complicated phase diagram is observed. The optimum temperature for the cocrystallization was determined to be 20°C.

When exposing the crystals with round edges to x-rays, the resolution of the diffraction was limited to ~20 Å, whereas crystals grown at 20°C showed x-ray diffraction to ~7 Å. A diffraction pattern of the latter crystals is shown in Fig. 2 *B*. Phase transitions of the detergent and PEG might be involved in this process. We made a test experiment to know whether this phase transition is reversible. We took crystals with sharp edges (grown at 20°C) and cooled them slowly down to 4°C. First, the edges of the crystals became round, later they changed their morphology into spheroids. The process was found to be irreversible. Increasing the temperature to 20°C did not lead to a significant change in either the morphology or the x-ray diffraction, which is not observed anymore. These results underline the complex phase behavior, which is observed in the simultaneous presence of a membrane protein complex, detergent, and PEG in the aqueous phase, as mentioned above. To elucidate the structural constraints of the spheroids, electron microscopy or atomic force microscopy could be used in future experiments.

Degree of supersaturation/homogeneous/heterogeneous nucleation

Crystallization was performed by vapor diffusion using "hanging drop" techniques. The concentration of the effectors (salt, PEG, and buffer) in the reservoir of 900 μl is two to three times higher than the concentration in the protein containing drop of 3 μl. Equilibration was achieved after 4 days at 20°C and, after complete equilibration, the protein concentration was four times higher than the protein concentration of a saturated solution (supersaturation of 4). Large single crystals of a diameter >0.5 mm were necessary for the EPR investigations. We achieved the growth of larger single crystals as follows.

The 3 μl drops containing 90 μM PSI, 100 μM ferredoxin, 4.75% PEG 400, 50 mM $CaCl_2$, 34 mM MES pH 7.5, and 0.02% β-DM were placed on a siliconized glass plate and equilibrated against a reservoir of 900 μl precipitant solution containing 14% PEG 400, 150 mM $CaCl_2$, and 100 mM MES. After the beginning of vapor diffusion, the crystallization chambers were opened at various times (between 6 h and 3 days) for time periods of 1 to 30 s. This procedure induced a partial higher supersaturation at the surface of the protein drop, leading to the induction of homogeneous nucleation. The optimal conditions were determined to be an opening of the chambers after a 24 h equilibration time for 5 s. One to five crystals were observed per drop after a further 2 days of equilibration. In some cases, one large crystal (diameter 0.3–1.0 mm, height of the plate 0.2–0.5 mm) is located in the middle of the drop, which is compact and can be used for spectroscopic and EPR investigations.

Whereas the EPR investigations on the single crystals presented in this work led to deeper insights into the arrangement of the FeS clusters and into the crystal geometry, x-ray structure analysis of the crystals was so far limited by a mosaic spread of the crystals of >2°. Improvement of the x-ray diffraction quality might be achieved in the future by the use of seeding techniques. Nucleation problems influence the cocrystallization of the PSI/ferredoxin complex, as is the case for PSI_a. Reduction of the mosaic spread can be achieved by induction of nucleation by combined microseeding and macroseeding techniques (Fromme and Witt, 1998). As a prerequisite for the seeding techniques, the determination of the complete phase diagram of the solubility of the PSI/ferredoxin complex is in progress.

Light exposure during inspection and mounting of the crystals might be another limitation for the x-ray diffraction quality of the crystals. After charge separation, reduction of ferredoxin may reduce the binding constant, so that it could leave the binding site. As ferredoxin could be involved in the crystal contacts, absorbed photons may induce defects in the cocrystals via ferredoxin dissociation. Such a phenomenon would explain the following observations: when cocrystals are exposed to white light at room temperature, the edges of the crystals become round after 5 min and under high light intensity, small cocrystals can even dissolve. We therefore inspected and mounted the crystals under weak green light. However, we cannot exclude that this low-light exposure limits the resolution and increases the mosaic spread.

Stoichiometry of photosystem I and ferredoxin

From EPR data (see below), the stoichiometry of PSI and ferredoxin in the cocrystals has been estimated to be ~1:1. Further evidence for this stoichiometry was provided by observations of crystal formation with different PSI/ferredoxin stoichiometries during crystallization. When ferredoxin was present in equimolar amounts or exceeded the amount of PSI, exclusively orthorhombic crystals were observed. However, when PSI exceeded the amount of ferredoxin, i.e., with a ratio of 0.6–0.8 ferredoxin to one PSI, the following behavior was observed: at first, orthorhombic

crystals containing the PSI/ferredoxin complex grew in 1–2 days in the protein solution. In a period of 4 days to 1 week, thin hexagonal needles were observed in addition to the already existing orthorhombic crystals. After dissolution of the orthorhombic crystals, SDS gel electrophoresis showed the presence of ferredoxin, which was clearly visible as an additional strong band, compared to electrophoresis of hexagonal crystals, which contained only PSI (data not shown). These results provide clear evidence that the orthorhombic crystal form is induced by ferredoxin binding to the PSI complex and that these crystals probably contain a 1:1 complex of PSI with ferredoxin.

Cocrystal characterization

X-ray diffraction data were first collected at room temperature at beamline SRS 9.6 at the Synchrotron in Daresbury, UK, and more recently at beamline ID14 at ESRF in Grenoble. The crystals diffract x-rays to a resolution of 7 Å (see Fig. 2 *B*); However, the crystals show decrease of diffraction quality during x-ray exposure, so that the data could be evaluated only to a resolution of 9 Å. Preliminary data evaluation revealed a space group of $P2_12_12_1$ with unit cell dimension of $a = 194$ Å, $b = 208$ Å, and $c = 354$ Å. However, due to the high mosaic spread of the crystals, the space group could not be determined unambiguously so that the $P2_12_12$ and $P2_122$ space groups could not be excluded. The orthorhombic space group of the crystals implies that each unit cell contains four trimers. The solvent content was estimated to be 64%, which is much smaller than the solvent content of the PSI_a crystals of 78% (Fromme and Witt, 1998).

Powder-type EPR spectra of the cocrystals

Fig. 3 exhibits powder-type EPR spectra of cocrystals, which were obtained from two different EPR tubes containing a large number of small cocrystals. Both samples were prepared under highly reducing conditions (an excess of sodium dithionite and methyl viologen) as described in Materials and Methods and were frozen under dim room light. Spectra *A* and *B* were recorded at 8 and 45 K, respectively, from a sample prepared at pH 9.2 and which was not further illuminated. Spectrum *B* exhibits *g*-values of ~1.885, 1.955, and 2.05, which can be ascribed to the reduced [2Fe-2S] cluster of ferredoxin. F_A^- and F_B^- are expected to be hardly visible at this temperature due to severe line-broadening (see, e.g., Lelong et al., 1994). The spectrum of a frozen solution of ferredoxin recorded under similar conditions is indistinguishable from spectrum *B*. In spectrum *A*, the main lines are observed at *g*-values of ~1.86, 1.89, 1.945, and 2.05. These signals correspond to the reduced forms of the [4Fe-4S] clusters of PSI: the *g*-value at 1.86 is due solely to F_A^-, whereas F_A^-, F_B^-, and (F_A^-, F_B^-) contribute to various extents to the other lines

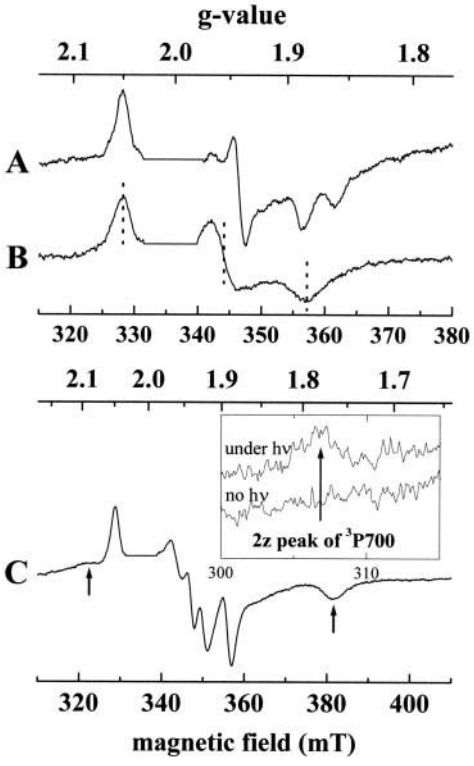

FIGURE 3 Powder-type EPR spectra of cocrystals obtained from samples containing a large number (>50) of small cocrystals. Spectra *A* and *B* were obtained with a sample prepared in the crystallization medium at pH 9.2, with 15 mM sodium dithionite and 200 μM methyl viologen. The sample was incubated at room temperature for 5 min in the presence of argon and was frozen under dim room light. The dotted vertical lines in spectrum *B* correspond to $g = 1.885$, 1.955, and 2.05, respectively. These resonances were ascribed to reduced ferredoxin. Spectrum *C* was obtained from another sample prepared under conditions similar as above except pH = 8.3. After freezing, the sample was illuminated at 240 K for 2 h with white light from a 800 W tungsten-halogen lamp. The vertical arrows ($g \approx$ 1.765 and 2.09) were ascribed to F_X^-. For spectra *A–C* the large radical signals around the $g = 2$ region were erased for easier data display. The inset shows the spectrum recorded on the same sample under and after illumination at low field (between 300 and 315 mT). EPR conditions (temperature, microwave power, and modulation amplitude at 100 kHz, respectively): spectrum *A*, 8 K, 80 mW, 1 mT; spectrum *B*, 45 K, 20 mW, 1 mT; spectrum *C*, 9 K, 80 mW, 1 mT; *inset:* 4.2 K, 0.2 mW, 2.1 mT.

(1.89, 1.945, and 2.05). Under the EPR conditions used for measuring this spectrum (8 K and 80 mW of microwave power), only a small signal is observed at $g \approx 1.96$, indicating that the ferredoxin signal is highly saturated. When the spectrum is recorded at 15 K, a distinct shoulder is observable at $g \approx 2.064$ (not shown), which can be ascribed to F_B^-. This signal is not visible in spectrum *A* presumably because of microwave power saturation.

The lower part of Fig. 3 shows the spectra measured with another sample that was prepared at pH 8.3 and was illuminated at 240 K for 2 h with white light. Spectrum *C* was recorded at 9 K and high microwave power (80 mW) to enhance signals due to F_X^-, which are indicated by vertical

arrows ($g \approx 1.765$ and 2.09). The other spectral features in between are due to the coupled (F_A^-, F_B^-) signal. Reduced ferredoxin may contribute to features around 1.89 and 2.05 and is distinctly observed as a $g \approx 1.96$ signal. The ferredoxin spectrum was also measured at 45 K, giving a spectrum similar to spectrum *B*. It must be also emphasized that the *g*-values and the linewidths of the spectra *A* and *C* shown in Fig. 3 are indistinguishable from those found for the PSI iron-sulfur centers F_A^-, F_B^-, and F_X^- in a frozen PSI solution.

When studied under illumination at 4.2 K, a small signal is observed around 3066 G, as shown in the inset of Fig. 3 (spectrum "under hν"). A similar signal is observed at high field in a symmetrical position compared to the $g_{\text{free electron}}$ position (not shown). These features can be ascribed to a chlorophyll triplet state signal exhibiting a zero-field splitting parameter $|D|$ of 0.0282 cm^{-1}. Similar features (with $|D| \approx 0.028$ cm^{-1}) have been previously shown to arise from the P700 triplet state at low temperature (Rutherford and Mullet, 1981). Therefore, we tentatively ascribe the observed signal to the low-field peak (2z) of the ^{3}P700 state. This signal is rather small, which may be explained by the weak stationary concentration of the excited state under continuous illumination of the dark cocrystals. The ^{3}P700 state exhibits four other innermost peaks, which were not observed in our experiments. This may be due to the fact that the outermost peaks of ^{3}P700 observed under stationary conditions are much larger than the innermost features, which makes these last ones unobservable under our experimental conditions. If one assumes that the ^{3}P700 state is formed, it would indicate that the secondary acceptor, the phylloquinone A_1, has been prereduced in some PSI centers (Bonnerjea and Evans, 1982).

Both samples were used for a quantitative estimate of ferredoxin stoichiometry in the cocrystals (see Materials and Methods). The ferredoxin/PSI ratios were found to be 0.85 ± 0.1 and 0.95 ± 0.1 for the two samples, respectively.

Illumination of PSI at low temperature under moderate redox conditions is known to lead to the formation of $P700^+$ and $(F_A, F_B)^-$ with the preferential photoreduction of F_A in most cases (see, e.g., Brettel, 1997). This charge separation was studied in a third sample containing many small cocrystals, which was prepared at pH 7.5 in the presence of ascorbate and DCPIP. The sample was frozen in darkness to maintain P700 reduced and the iron-sulfur clusters oxidized. The light-induced spectrum was recorded at 25 K. Except for a large signal around $g = 2.0$ due to $P700^+$, the largest signals at $g = 1.864$, 1.943, and 2.049 are ascribed to F_A^-. Spectral features due to F_B^- are observable at *g*-values around 1.88, 1.93, and 2.07 (not shown).

EPR study of single cocrystals: preliminary characterization of the light-induced spectra

For this report, two different cocrystals were studied in detail for light-induced spectra at 10–20 K. Illumination of PSI at low temperature under moderate redox conditions leads to the formation of $P700^+$ and $(F_A, F_B)^-$ with the preferential photoreduction of F_A. The presence of ferredoxin at its binding site in a covalent complex was found to decrease the amount of F_B^- relative to F_A^- (P. Sétif, unpublished observation). Thus we expected a small contribution of F_B^- in the light-induced spectra. Moreover, this contribution was decreased in a series of experiments made at 10 K and 20 mW of microwave power, for which a stronger saturation of the F_B^- signal compared to that of F_A^- is expected, in line with the relaxation properties of the two clusters (Rupp et al., 1979). These experiments will be described and interpreted first. Nonsaturating conditions were also used (20 K, 5 mW), in which the relative contribution of F_B^- is increased. These experiments will be described further below.

A complete orientation pattern was obtained at 10 K by recording difference spectra at many θ_1 and ϕ_1 angles. This was composed of different datasets, each dataset being obtained by varying θ_1 from 0 to 180° and keeping the ϕ_1 angle fixed (see Fig. 1 for a scheme of the crystal holder). From the crystallographic data, the space group has been found to be orthorhombic and the unit cell dimensions have been determined (see above). However, the present crystallographic data did not allow the derivation of the orientation of the C_3 trimeric axis in the unit cell (*a*, *b*, *c*) framework. As an initial guess for interpreting the EPR spectra, it was hypothesized that all C_3 axes were parallel, as is the case in PSI_a crystals (Krauss et al., 1993). If this would be the case, there should be a particular (ϕ_1, θ_1) orientation with the C_3 axis parallel to the magnetic field, and this should result in a single F_A^- line (see, e.g., Brettel et al., 1992). We searched systematically for such a special orientation of cocrystals. This was done for the two different cocrystals by recording light-induced EPR spectra and varying the two angles ϕ_1 and θ_1 from 0 to 180° by steps of 10–15° and 5°, respectively. With both cocrystals, it was not possible to observe a single line due to F_A^- at any value of (ϕ_1, θ_1). Several possibilities can be considered to explain these observations: 1) It might be speculated that the right (ϕ_1, θ_1) orientation was not found because the two angles were not adjusted with a sufficient precision or because of a large mosaic spread. We estimated that this was very unlikely because a misalignment of up to 10° between the C_3 direction and the magnetic field is not expected to give rise to several lines, but only to broaden the F_A^- single line, which should lie at $g = 1.931$–1.935 (Brettel et al., 1992; Kamlowski et al., 1997). 2) One might have to abandon the above hypothesis that all C_3 axes of PSI trimers are parallel to each other in a single cocrystal. In the following it will be shown, from a detailed characterization of the orientation dependence of the signal due to F_A^-, that this is the case, i.e., C_3 trimer axes are not parallel one to each other in the PSI/ferredoxin cocrystals.

During the course of the EPR measurements, several characteristics of the light-induced spectra due to F_A^- were noteworthy. First, in some orientations, up to 10 different lines could be resolved. For the whole set of data, a minimum number of three different lines were observed. Second, for several (ϕ_1, θ_1) orientations, one line was observed that was isolated from the others (either in the low- or high-field region of the spectrum). After double integration, this line was found to correspond to ~1/12 (between 1/11 and 1/14) of the whole integrated intensity of iron-sulfur centers. These observations are consistent with the presence of four PSI trimers in the unit cell, giving rise to 12 different lines due to 12 magnetically inequivalent F_A^- for a random cocrystal orientation. However, a smaller number of lines (between 3 and 10) was generally observed, presumably because of overlapping. Because of this large number of overlapping lines, it was not possible to follow reliably a given resonance at varying orientations. For further interpretation of the EPR data we chose to use another strategy, which is summarized in the next paragraphs, with details given in the Appendix.

We also observed EPR signals of reduced ferredoxin in single cocrystals. Such data were obtained with cocrystals that were reduced at room temperature at very low redox potentials in the presence of methylviologen. In such cocrystals, large signals due to F_A^- and F_B^- were always present. For an unambiguous identification of ferredoxin signals, it was therefore necessary to perform the EPR measurements at 40–50 K. This allowed us to observe specifically ferredoxin signals, as the F_A^-/F_B^- signals are considerably lifetime-broadened at this temperature. However, the signals thus obtained are considerably noisier than those ascribed to F_A^- and F_B^-, which are discussed in the present paper. This has two different origins: first, the ferredoxin signals at 40–50 K are broader and their amplitude is smaller than the F_A^-/F_B^- signals recorded at 8–20 K (see, e.g., Fig. 3); second, no baseline could be subtracted for such lines, contrary to the light-induced spectra shown below. This led to broad and poorly resolved ferredoxin signals (not shown).

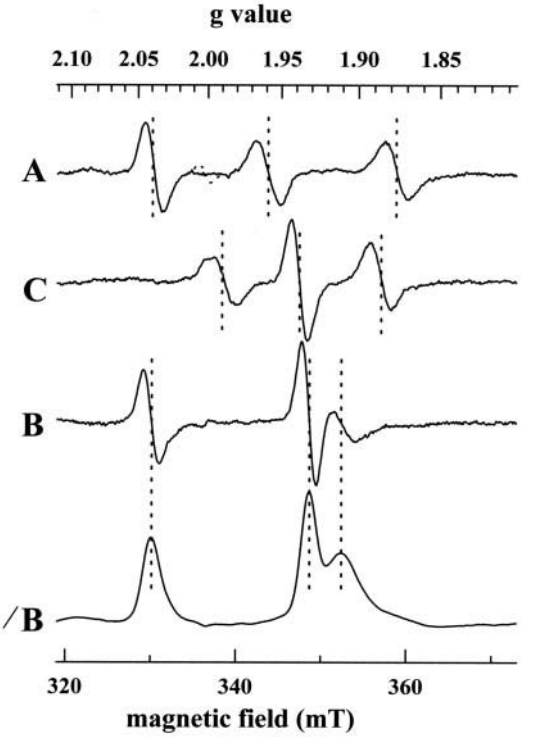

FIGURE 4 Light-induced spectra recorded at 10 K for a single cocrystal at three mutually perpendicular orientations. Spectra *A–C* were recorded for (ϕ_1, θ_1) = (0°, 40°), (0°, 130°), and (90°, 5°), respectively. The $P700^+$ signal is shown as a dotted line around $g = 2.00$ in spectrum *A* and was subtracted from all three spectra. The nine F_A^- resonances that were used for characterizing its *g*-tensor are indicated as dotted vertical lines and their numerical values are given in Table 1. Integration of spectrum *B* gave spectrum /*B*. The right part of this spectrum was used for fitting with two Gaussian lines (not shown). EPR conditions: temperature, 10 K; microwave power, 20 mW; modulation amplitude at 100 kHz, 1 mT.

Characterization of F_A^- resonances at three particular orientations

As mentioned above, a minimum number of three lines was found at some particular orientations for the two cocrystals that were studied. For each of the cocrystals, spectra comprising three lines were found at three different (ϕ_1, θ_1) orientations. The three corresponding spectra were identical for both cocrystals and are shown in Fig. 4 for one of these cocrystals. The (ϕ_1, θ_1) angles associated to these spectra correspond to mutually perpendicular orientations (see legend to Fig. 4). For interpreting these spectra, the hypothesis that all C_3 axes of the trimers are parallel was relaxed; in the cocrystal, the C_3 axis of a given trimer was considered to make angles χ_a, χ_b, and χ_c with respect to the cocrystal axes *a*, *b*, and *c*, respectively (Fig. 5 *A*; (*A*, *B*, *C*) is a permutation of (*a*, *b*, *c*)). When taking into account the point group of the cocrystals (222 corresponding to the orthorhombic space group), the squares of the direction cosines between all C_3 axes and (*a*, *b*, *c*) should be identical. Moreover, the squares of the direction cosines between the *g*-tensor principal axes and (*a*, *b*, *c*) should be identical for one PSI of a trimer and the corresponding PSI of another trimer resulting from a rotation about a unit cell axis. For cocrystal orientations for which one of the unit cell axes is parallel to the magnetic field, the EPR spectrum of a single EPR species should therefore consist of three different lines due to the three different PSIs in one trimer. The three lines observed in the spectra of Fig. 4 might therefore originate from the three magnetically inequivalent F_A^- species in the three different PSI reaction centers of a given trimer, when either the *a*, *b*, or *c* axes are parallel to the magnetic field.

Nine different *g*-values (*dotted lines*) were derived from the three spectra of Fig. 4 (*A*, *B*, and *C*). The *g*-values of the two high-field lines of spectrum *B* were obtained after

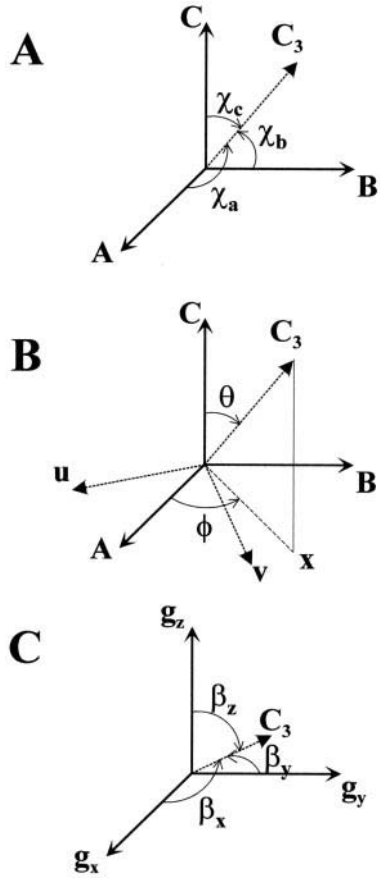

FIGURE 5 Angular parameters used for characterizing the orientation of the C_3 trimer axis in the (A, B, C) framework (parts A and B) and in the (g_x, g_y, g_z) framework (part C). (A, B, C) is an arbitrary permutation of (a, b, c), with a, b, and c being the three mutually perpendicular unit cell axes. (B) (u, v, C_3) is an orthonormal framework. The u and x axes lie in the (A, B) plane. The C, C_3, v, and x axes lie in the same vertical plane.

integration of the signal (spectrum /B) and fitting with two Gaussian lines (not shown). Among the nine different lines, two of them deserve special mention: 1) the high-field line of spectrum B is fairly broad. It was unsuccessfully tried to get it narrower by small changes in the (ϕ_1, θ_1) angles. It will be shown below that this can be easily explained by a small misalignment and/or by mosaic spread. 2) The low-field peak of spectrum C exhibits some structure. This may have two different origins. First, this line is close to $g = 2$ and subtraction of $P700^+$ might not be perfect; second, it will be shown below that this probably results also from a slight misalignment. The nine resonances thus identified and ascribed to F_A^- are given in Table 1.

Determination of the orientation of the C_3 axis and of the g-tensor of the cluster F_A

The above g-values were measured with a precision of <0.001 except for the low-field resonance of spectrum C (± 0.004). In the following, it is therefore assumed that the three g-values of spectrum A (called set A of g-values; idem for set B and set C) correspond to the resonances of F_A^- in the three PSIs of a given trimer when one unit cell axis, denoted A, is parallel to the magnetic field (idem for B and C). As EPR cannot help in identifying A, B, or C to any unit cell axis, (A, B, C) is an unknown permutation of (a, b, c).

TABLE 1 Three different sets of three resonances observed at three mutually perpendicular cocrystal orientations (see Fig. 4)

Spectrum	g-Values	Square of g-Values
A	2.038/1.962/1.876	4.153/3.848/3.521
B	2.040/1.932/1.909	4.162/3.731/3.646
C	1.988/1.939/1.887	3.952/3.760/3.561

By using a minimization procedure described in detail in the Appendix, these nine resonances were sufficient to derive: 1) the two angles (ϕ, θ) which relate the framework (u, v, C_3) to the framework (A, B, C): $\phi = 36.5°$; $\theta = 23.0°$. These angles correspond to the following angles between C_3 and the unit cell axes (see Fig. 5): $\chi_A = 71.7°$; $\chi_B = 76.6°$; $\chi_C = 23.0°$; 2) the principal values of the F_A^- g-tensor: $g_x = 1.864$; $g_y = 1.9405$; $g_z = 2.050$; and 3) the unitary transformation between the orthonormal frameworks (A, B, C) and (g_x, g_y, g_z). The three Euler angles for transforming (A, B, C) into (g_x, g_y, g_z) are 185.7°, 106.7°, and 23.3°, respectively. From these angles and the (ϕ, θ) angles, one can also derive the angles between C_3 and the principal directions of the F_A^- g-tensor (see Fig. 5): $\beta_x = 51.4°$; $\beta_y = 50.6°$; $\beta_z = 62.9°$.

It can be noted that the above parameters, including the principal g-values of the F_A^- g-tensor, were obtained solely from the minimization procedure. The values obtained herein for the F_A^- g-tensor are close to what was determined before from the study of PSI_a crystals and to the values obtained from the powder spectrum of cocrystals (Brettel et al., 1992; Kamlowski et al., 1997; see Table 2 for comparison), thus strongly supporting our calculations.

Simulation of rotation patterns of F_A^-

By taking into account the parameters derived above together with the knowledge of the (A, B, C) axis system in the laboratory framework, it is possible in principle to simulate any set of data. This is shown in Fig. 6 for one dataset for which the predicted positions of the lines were compared to the experimental light-induced difference spectra. This dataset was obtained with the same cocrystal that was assumed to have a peculiar orientation with the B axis almost parallel to the bottom plane of the crystal holder (Fig. 1). In such a case, it is possible to adjust the ϕ_1 angle so that B lies vertically. This was performed for $\phi_1 = 0$. In this configuration, the two directions A and C could be made parallel to the magnetic field within the same dataset (for $\theta_1 = 40°$ and 130°; see arrows marked A and C).

TABLE 2 *g*-Tensor characteristics of the reduced clusters F_A^- and F_B^- of *Synechococcus elongatus* PSI

	g-Values of the Cluster			Angles with the C_3 Axis			
	g_x	g_y	g_z	β_x	β_y	β_z	Reference
F_A^-	1.864	1.9405	2.050	51.4°	50.6°	62.9°	This work
F_A^-	1.864	1.943	2.049	—	—	—	This work (powder spectrum of cocrystals)
F_A^-	1.8665	1.9485	2.0535	52.4°	48.7°	64.1°	Brettel et al., 1992*†
F_A^-	1.856	1.941	2.051	53°	48°	64°	Kamlowski et al., 1997†
F_B^-	1.877	1.931	2.068	72°	56°	40°	This work
F_B^-	1.880	1.916	2.056	77°	60°	34°	Kamlowski et al., 1997†

*Average values reported for trimers I and II.
†In Brettel et al., 1992 and Kamlowski et al., 1997 the angles are given with respect to the crystallographic *c*-axis, which is considered to coincide with the C_3 trimer axis.

Several features emerge from this figure:

1. The calculated *g*-values (*continuous lines*) satisfactorily match the observed spectra. However, small deviations between experimental and calculated *g*-values are seen (see spectra at $g \approx 1.95$ for θ_1 around 10 and 70°). This discrepancy is not understood at the moment;

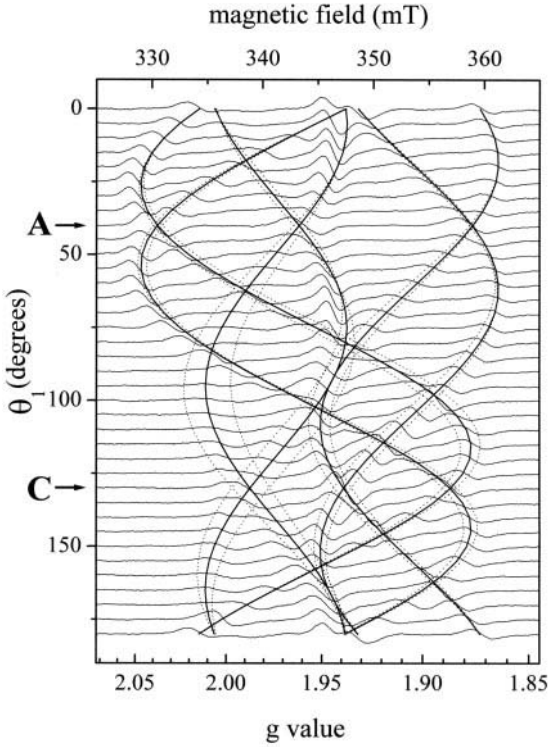

FIGURE 6 Light-induced spectra recorded at 10 K. This series of spectra was recorded with the same cocrystal used for Fig. 4. The angles are $\phi_1 = 0$ and $\theta_1 = 0$ to 180° by steps of 5°. The spectra *A* and *C* (*arrows*) correspond to those exhibited in Fig. 4. The continuous lines are simulated *g*-values assuming that the *B* axis lies perfectly vertical during the whole series, which results in six different resonances at any orientation. The dotted lines were simulated by taking into account that the *B* axis is not perfectly vertical, which results in some splitting of all six lines (see text). Same EPR conditions as in Fig. 4.

2. Only six different lines were observed. This peculiar situation is ascribed to the fact that the *B* axis lies almost vertically for the whole dataset. In such a case, two different PSIs related by the twofold rotation around this axis are magnetically equivalent. This is expected to result in a twofold decrease in the number of lines, as found and simulated in Fig. 6. However, the *B* axis is not perfectly vertical. This was simulated by taking into account this small deviation. Splitting of the six lines that are expected for *B* being perfectly vertical is expected. This is shown by the dotted lines in Fig. 6. Such a splitting may contribute to the structure observed for the low-field peak of spectrum *C* (see Fig. 4; $\theta_1 = 130°$ in Fig. 6);
3. Sets of data recorded at other ϕ_1 angles were also satisfactorily fitted with the above parameters (not shown). In these cases, 12 lines are generally expected. Taking into account the crowding and fortuitous overlapping of lines, this was consistent with the experimental spectra for which up to 10 distinguishable lines were observed.

Determination of the *g*-tensor of the cluster F_B

F_B^- signals in a single cocrystal were studied at 20 K and 5 mW of microwave power. Under these conditions, the size of the F_B^- signals was relatively enhanced compared to the conditions used above, but only a few F_B^- signals of significant amplitude could be identified. These signals, which were recorded with the same cocrystal used for studying F_A^- (Figs. 4 and 6) are shown in Figs. 7 and 8 together with the large F_A^- signals. Fig. 7 exhibits the spectra recorded at the three orientations for which one of the unit cell axes is assumed to be parallel to the magnetic field. The $P700^+$ contributions were not subtracted, contrary to Fig. 4, and this results in large signals around $g \approx 2.00$. Apart from this $P700^+$ contribution, only one supplementary signal for each orientation was observable compared to the spectra of F_A^- shown in Fig. 4. These signals, which are indicated by vertical arrows and are marked as g_A, g_B, and g_C, are ascribed to F_B^-. The g_A and g_C signals are clearly visible at values of 1.909 and 2.048, respectively. The g_B signal, which is more difficult to observe around $g = 1.885$, is also

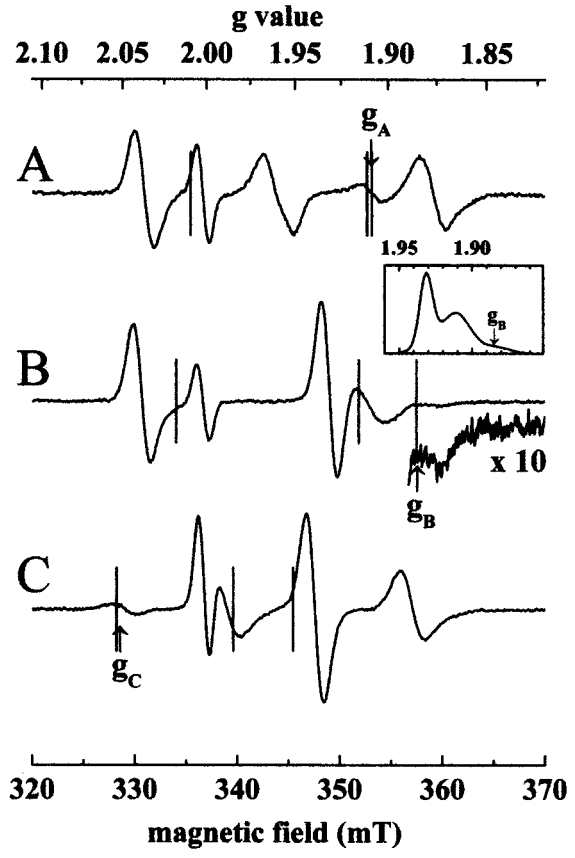

FIGURE 7 Light-induced spectra recorded at 20 K and 5 mW of microwave power for the same cocrystal and the same mutually perpendicular orientations as those used in Fig. 4. The resonances at $g_A = 1.909$, $g_B = 1.885$, and $g_C = 2.048$ (*arrows*) were ascribed to F_B^-. These three *g*-values were used for characterizing the F_B^- *g*-tensor together with a few resonances ascribed as well to F_B^- and shown in Fig. 8 ($g = 2.067$ at (ϕ_1, θ_1) = (0, 110°) and (0, 150°); $g = 2.063$ at (ϕ_1, θ_1) = (0, 85°) and (0, 175°); $g = 2.061$ at (ϕ_1, θ_1) = (0, 75°) and (0, 185°). This was performed by a systematic parameter search for minimizing the sum of the deviations between the above-observed six resonances (at 1.909, 1.885, and 2.048 for sets *A*, *B*, and *C*, respectively; at 2.067, 2.063, and 2.061 for (ϕ_1, θ_1) = (0, 110°), (0, 85°), and (0, 75°), respectively) with the calculated ones. For this minimization, we use the orientation of the C_3 axis that we determined from the study of F_A^-. The following parameters were varied: $g_x = 1.88 \pm 0.05$; $g_y = 1.93 \pm 0.05$; $g_z = 2.07 \pm 0.05$; all possibilities for the angles defining the orientations of the F_B^- *g*-tensor in the (*A*, *B*, *C*) framework. The minimization output was used for deriving the properties of the F_B^- *g*-tensor (see text and Table 2) and the three F_B^- resonances that are expected for each of the three orientations with *A*, *B*, or *C* parallel to the magnetic field. These calculated resonances are shown as thin vertical lines in Fig. 7 (set *A*, $g = 1.9085, 1.911, 2.009$; set *B*, $g = 1.885, 1.915, 2.018$; set *C*, $g = 1.951, 1.985, 2.054$).

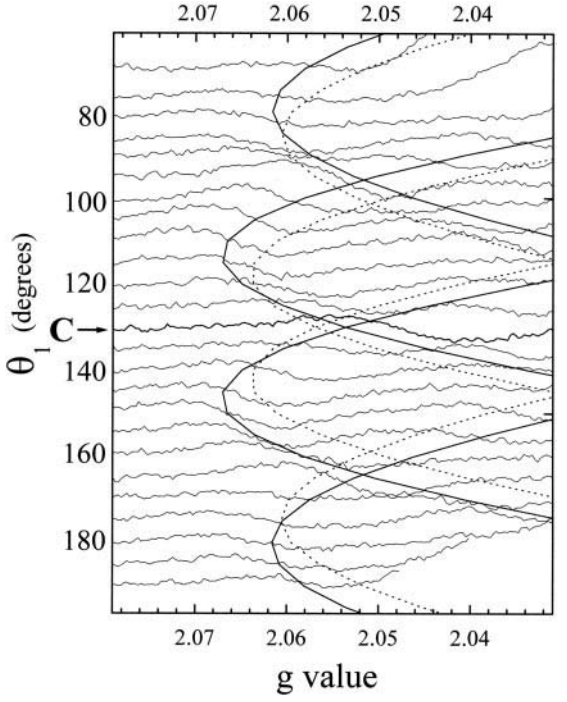

FIGURE 8 Light-induced spectra recorded at 20 K and 5 mW of microwave power. This series of spectra was recorded with the same cocrystal used for Figs. 4 and 6 and at similar orientations as those used in Fig. 6. The angles are $\phi_1 = 0$ and $\theta_1 = 70$–190° by steps of 5°. The continuous lines are simulated *g*-values assuming the properties of the F_B^- *g*-tensor (Table 2), which were calculated in the present report from the best-fitting procedure described in the legend to Fig. 7. The same six observed resonances as those described in Fig. 7 were best-fitted assuming the orientation of the F_B^- *g*-tensor that is reported in Kamlowski et al. (1997) (bottom line in Table 2) and by taking the principal F_B^- *g*-values as free parameters ($g_x = 1.88 \pm 0.05$; $g_y = 1.91 \pm 0.05$, and $g_z = 2.05 \pm 0.05$). The best fit was obtained for $g_x = 1.878$, $g_y = 1.932$, and $g_z = 2.064$ and the dotted lines are simulated *g*-values assuming these principal *g*-values together with the orientation reported in Kamlowski et al. (1997).

expanded 10-fold. Fig. 8 exhibits the low-field features, observed at $g \approx 2.045$–2.067, which are found with the *B* axis being vertical ($\phi_1 = 0°$) and $\theta_1 = 70$–190°. Identical orientations were used for studying F_A^- (Fig. 6). As is the case for F_A^-, a mirror symmetry is observed around $\theta_1 = 130°$ (the *C* axis being parallel to the magnetic field). The highest *g*-values were observed at $g = 2.067$ for $\theta_1 = 110$ and 150°. A relative maximum of *g*-value was also found at 2.063 for $\theta_1 = 85$ and 175°; *g*-values of F_B^- in the cocrystal were found around 1.88, 1.93, and 2.07 from the powder spectrum (not shown). These approximate values (±0.05), together with the orientations of the C_3 axes in the (*A*, *B*, *C*) framework, were used for simulating the signals at g_A, g_B, and g_C (Fig. 7) as well as the angular dependence of the low-field *g* signals of F_B between 2.045 and 2.067 (Fig. 8). This was done via a minimization procedure, which is detailed in the legend to Fig. 7 and resulted in the following characteristics of the F_B^- *g*-tensor (cf. Table 2): 1) the principal values $g_x = 1.877$, $g_y = 1.931$, $g_z = 2.068$ are much closer to the *g*-values generally observed for F_B^- (see, e.g., Jung et al., 1996; $g_{x,y,z} = 1.880, 1.930, 2.069$) than those that were found in a previous study on PSI_a crystals (Kamlowski et al., 1997); 2) the angles between the C_3 axis and the principal directions of the *g*-tensor: $\beta_x = 72°$; $\beta_y = 56°$; $\beta_z = 40°$ (see definitions in Fig. 5) slightly differ from the values found in PSI_a crystals (Kamlowski et al., 1997).

From the above characteristics, it was possible to derive the F_B^- resonances that are expected for the three preferential orientations with C_3 parallel to *A*, *B*, or *C*. These resonances are indicated in Fig. 7 by vertical lines (see legend for numbers). It was also possible to simulate the orientation pattern corresponding to the low-field F_B^- resonances shown in Fig. 8 (*continuous lines*). This pattern can be compared with the best-fit pattern that could be obtained from the angular characteristics of the F_B^- *g*-tensor derived from the data on PSI_a in Kamlowski et al. (1997) by taking the principal *g*-values as free parameters. This pattern is shown as dotted lines in Fig. 8 (see figure legend for details on the fitting procedure and the principal *g*-values found for the best fit). From the comparison of both types of fits, we conclude that the angular parameters that are derived in the present work ($\beta_{x,y,z} = 72°, 56°, 40°$) are more satisfactory that those found in Kamlowski et al. (1997). The slight deviations between the two sets of angles (up to 6°) thus appear to be significant and could be ascribed to a slight modification of the F_B orientation due to the presence of ferredoxin. However, one cannot exclude that these small deviations ($\leq 6°$) are due to the uncertainties inherent to the EPR analyses of (co)crystals.

DISCUSSION

In chloroplasts and cyanobacteria, ferredoxin associates reversibly to the reaction center of photosystem I (PSI). Within the complex, ferredoxin is photoreduced in the submicrosecond-microsecond time range (Sétif, 2001) before it dissociates for later interaction with other soluble electron acceptor proteins. Only a few examples of structures of reversible complexes between electron transfer proteins are known to date (Pelletier and Kraut, 1992; Chen et al., 1992, 1994; Adir et al., 1996; Morales et al., 2000; Kurisu et al., 2001; Lange and Hunte, 2002). Among these, the x-ray structure of cocrystals formed between ferredoxin and ferredoxin-$NADP^+$ reductase has been recently determined by two different groups (Morales et al., 2000; Kurisu et al., 2001). For the complex between photosystem I and ferredoxin or flavodoxin there is no x-ray structure available.

The present paper reports for the first time the cocrystallization of PSI with ferredoxin, both being purified from cyanobacteria, i.e., from *Synechococcus elongatus* and *Synechocystis* 6803, respectively. PSI is in the trimeric form, as in PSI_a crystals used for structure determination at 2.5 Å resolution (Jordan et al., 2001). A number of PSI mutations were used for identifying a docking region for ferredoxin (reviewed in Sétif, 2001), in accordance with a simulated docking model based on the 6 Å structure (Fromme et al., 1994) and with modeling studies using electrostatic potentials for the structural alignment (Ullmann et al., 2000). The interface between both partners presents the peculiarity that at least the three different extrinsic stromal subunits and probably extrinsic loops of PsaA of PSI are involved in ferredoxin binding. The determination of the structure of the complex between PSI and ferredoxin is important for the understanding of the protein-protein interaction and the inter-protein electron transfer, because this will allow the PSI/ferredoxin interface to be characterized in greater detail and the possible participation of other PSI subunits in ferredoxin binding to be identified. The first steps toward elucidation of this structure are reported here on cocrystals diffracting x-rays to a resolution of 7 Å. From our data, an orthorhombic space group was deduced with the unit cell dimensions $a = 194$ Å, $b = 208$ Å, and $c = 354$ Å, which leads to four different PSI trimers, i.e., 12 PSI monomeric functional subunits present in the unit cell.

The cocrystals were characterized by EPR at low temperature

First, samples consisting of a large number of small cocrystals were studied after various redox and illumination pretreatments, which gave rise to powder-type EPR spectra. In these experiments, the EPR signatures of all three iron-sulfur clusters of PSI (F_A, F_B, and F_X) were observed, as well as the EPR spectrum of the reduced [2Fe-2S] cluster of ferredoxin. Under highly reducing conditions it was also possible to observe the triplet state of P700 under continuous illumination. These data indicate that the cocrystals are much more resistant than the PSI_a crystals. During the last several years, the use of spectroscopic investigations on single PSI_a crystals led to a much deeper insight into the function, location, and structure of some of the cofactors (Brettel et al., 1992; Kamlowski et al., 1997, 1998; Bittl et al., 1997; Käss et al., 2001). However, spectroscopic investigations on single PSI_a crystals were limited by their instability. These cocrystals were grown at low ionic strength and show a solvent content of 80%. Moreover, only four salt bridges are involved in crystal contacts (Jordan et al., 2001; Fromme, 2002). The crystals dissolve immediately by addition of redox compounds such as dithionite, or at pH above 7, so that only a limited number of redox states of the cofactors could have been investigated.

In contrast, the PSI/ferredoxin cocrystals are much better suited to spectroscopic investigations because they are stable in the presence of many redox compounds in a pH range from 5.5 to 9.5. This property will be used in future experiments for studying various EPR species, such as the interaction spectrum of the [4Fe-4S] clusters F_A^- and F_B^- of PSI or the [2Fe-2S] cluster of ferredoxin. Values of 0.85 ± 0.1 and 0.95 ± 0.1 for the ferredoxin-to-PSI ratio were estimated for two different samples by spin quantitation of the ferredoxin signal. Growing crystals with a substoichiometric amount of ferredoxin led to the first appearance of PSI/ferredoxin cocrystals followed by the formation of PSI_a crystals. However, only PSI/ferredoxin crystals were obtained when ferredoxin was present in equimolar amounts or exceeded the amount of PSI. From both types of data it

appears very likely that the cocrystals are composed of 1:1 complexes of PSI and ferredoxin.

Second, the orientation-dependent pattern of the F_A^- EPR signal was studied in two different monocrystals at low temperature, F_A being the preferentially photoreduced acceptor during charge separation. From the available x-ray data it was not possible to measure unambiguously the orientation of the C_3 axis of trimeric PSI in the unit cell framework. This made the direct simulation of the orientation pattern by standard procedures unpractical, especially as the C_3 axes were found to be not parallel to any of the unit cell axes. This resulted in 12 magnetically inequivalent F_A^- clusters, i.e., 12 different EPR lines with partial overlapping, for a random orientation.

A new method was devised to deduce the orientation of the C_3 trimer axis with respect to the unit cell framework without any other input from the x-ray crystallographic analysis than the 222 point group of the unit cell. Hereby we were able to determine the orientation of the PSI/ferredoxin complex in the unit cell. Angles of (23°, 72°, 77°) were thus determined between C_3 and the unit cell axes. From EPR alone it is impossible to ascribe any of these angles to the *a*, *b*, or *c* unit cell axes. However, from the unit cell dimensions, the orthorhombic space group and packing considerations based on the dimension of the trimeric PSI from the recent x-ray structure (Jordan et al., 2001), it appears most likely that the unit cell axis closest to C_3 (at an angle of 23°) is the axis corresponding to the largest unit cell dimension, i.e., the unit cell axis *c* ($C = c$). As an intrinsic output of our method, we derived independently of any other data the *g*-values and the orientation properties of the F_A^- *g*-tensor. The angles between the principal axes of the F_A^- *g*-tensor and the C_3 axis were equivalent to those found previously in EPR studies of PSI_a crystals (Brettel et al., 1992; Kamlowski et al., 1997). This proves unambiguously the general validity of our approach. The full orientation pattern of the F_A^- signal could also be satisfactorily simulated.

By using the geometrical properties of the cocrystals derived from the study of F_A^-, it was possible to get the orientation of the F_B^- *g*-tensor despite the small EPR signal intensity ascribed to this signal. The *g*-values of F_B^- obtained from the powder spectrum of cocrystals were necessary to derive this information. The orientation of the F_B^- was thus found to be slightly altered compared to what was previously found in PSI_a (Kamlowski et al., 1997). Deviations of 4–6° were found between our data and those of (Kamlowski et al., 1997) for the angles between the C_3 axis of the trimer and the principal magnetic axes of F_B^-. At the moment, we cannot completely confirm that this reorientation is real because of the uncertainties in interpreting the EPR orientation patterns of a relatively small signal (compared to F_A^-) such as F_B^-. It can be noted, e.g., that the highest *g*-value found in Kamlowski et al., 1997 ($g_z = 2.056$) is quite different from what is generally known ($g_z \approx 2.07$) and from what is found in the present report ($g_z = 2.068$). This may be correlated to the difference observed in the angle between the C_3 and g_z axes between (Kamlowski et al., 1997) and our study. Another more appealing interpretation would be that the *g*-tensor of F_B^- slightly reorients upon ferredoxin binding. This would be linked to a reorientation of the binding pocket of F_B or a distortion of the [4Fe-4S] cubane geometry. The resolution of the cocrystal structure at a sufficient resolution and the comparison of F_B and its surrounding region in crystals and cocrystals might allow this hypothesis to be tested in the future.

APPENDIX

The *g*-tensor of F_A^- in the (*A*, *B*, *C*) framework

Determination of *g*-tensors in crystals involves construction of the $g \cdot g^T$ matrix, which is relevant to EPR measurements (g^T is the transpose matrix of *g*; see, e.g., Weil et al., 1994, pp. 87–91). The $g \cdot g^T$ matrix (denoted *gg* in the following for the sake of simplicity) is symmetrical and its trace is therefore invariant regardless of the orthonormal framework used. It is also orthogonally similar to a diagonal matrix corresponding to the principal directions of the *g*-tensor so that its trace is equal to the sum of the squares of the three *g*-values of the EPR species, F_A^- in this case.

The nine *g*-values given in Table 1 should therefore correspond to the diagonal elements of the *gg*-matrices of F_A^- in the three PSIs (denoted PSI_1, PSI_2, and PSI_3) of a given trimer in the (*A*, *B*, *C*) framework. The *gg*-matrix of PSI_1 can be defined as:

$$gg_1 = \begin{pmatrix} gg_{AA1} & gg_{AB1} & gg_{AC1} \\ — & gg_{BB1} & gg_{BC1} \\ — & — & gg_{CC1} \end{pmatrix}$$

The gg_1 matrix being symmetric, the terms below the diagonal have been omitted. From what precedes, gg_{AA1}, gg_{BB1}, and gg_{CC1} should be the squares of a *g*-value in set *A*, set *B*, and set *C*, respectively. gg_2 and gg_3 matrices of PSI_2 and PSI_3 are defined similarly, by taking other *g*-values in set *A*, set *B*, and set *C*. The traces of the three matrices gg_1, gg_2, and gg_3 should be the same, which leaves only one possibility for grouping the diagonal elements into three different matrices.

$$M_1 = gg_1 = \begin{pmatrix} 3.848 & gg_{AB1} & gg_{AC1} \\ — & 3.646 & gg_{BC1} \\ — & — & 3.952 \end{pmatrix}$$

$$M_2 = \begin{pmatrix} 3.521 & gg_{AB2} & gg_{AC2} \\ — & 4.162 & gg_{BC2} \\ — & — & 3.760 \end{pmatrix}$$

$$M_3 = \begin{pmatrix} 4.153 & gg_{AB3} & gg_{AC3} \\ — & 3.731 & gg_{BC3} \\ — & — & 3.561 \end{pmatrix} \quad (1)$$

The traces of the three above matrices are identical, within experimental errors

$$\sum_{I=A,B,C} gg_{II1} = 11.446 \qquad \sum_{I=A,B,C} gg_{II2} = 11.443$$

$$\sum_{I=A,B,C} gg_{II3} = 11.445$$

These values are similar to Σg^2 values of F_A^- that have been already found from crystallographic studies of PSI from *S. elongatus* (11.496–11.499 in Brettel et al., 1992; 11.419 in (Kamlowski et al., 1997)).

Constraints related to the C_3 symmetry of the PSI trimer

If one assumes that the three above matrices are the *gg* matrices of the three PSI reaction centers of a trimer with C_3 symmetry, they should be linked by simple relationships, as one PSI is related to another in the trimer by a rotation of $\pm 2\pi/3$ around the C_3 axis. In the following, Eul(α, β, χ) will denote a unitary rotation matrix defined by the three Eulerian angles α, β, and χ. The transformation from the (A, B, C) framework to the (u, v, C_3) framework is Eul(ϕ-π/2, θ, 0) (Fig. 5 *B*). One assumes that the (u, v) axes have a definite orientation relative to the PSI structure, i.e., for the three PSIs of a given trimer, one has the three different frameworks (u_1, v_1, C_3), (u_2, v_2, C_3), and (u_3, v_3, C_3), respectively. Because of the C_3 symmetry, (u_2, v_2, C_3) and (u_3, v_3, C_3) are transformed from (u_1, v_1, C_3) by Eul($\pm 2\pi/3$, 0, 0). It can be easily calculated that the following relationships hold among the matrices M_1, M_2, and M_3:

$$M_1 = U^{-1} \times M_2 \times U \quad \text{and} \quad M_3 = U \times M_2 \times U^{-1} \quad (2)$$

or

$$M_1 = U \times M_2 \times U^{-1} \quad \text{and} \quad M_3 = U^{-1} \times M_2 \times U \quad (3)$$

with the unitary matrix $U(\theta, \phi) = [\text{Eul}(\phi\text{-}\pi/2, \theta, 0)]^{-1} \times \text{Eul}(2\pi/3, 0, 0) \times \text{Eul}(\phi\text{-}\pi/2, \theta, 0)$. Equations 2 and 3 can be written as well:

$$U \times M_1 = M_2 \times U \quad \text{and} \quad M_3 \times U = U \times M_2 \quad (2')$$

$$M_1 \times U = U \times M_2 \quad \text{and} \quad U \times M_3 = M_2 \times U \quad (3')$$

Fitting procedure for determination of M_2

Equality 2 (or 3) corresponds to 12 independent equations, when the symmetry of matrices is taken into account and they comprise only 11 unknown parameters, i.e., the 9 off-diagonal elements of the M_i matrices and the 2 angles ϕ and θ that define the matrix U. Each of these two sets of equations is therefore overdetermined and should provide at most one solution. However, they are very complicated to solve directly and a strategy of best-fitting was chosen.

Step 1. The off-diagonal elements of the M_2 matrix were taken as adjustable parameters. M_2 was chosen as the starting matrix because its diagonal elements were best determined. It was first found that the absolute values of the off-diagonal elements cannot be larger than 0.4 (this is true as well for M_1 and M_3). This can be easily checked by calculating the *gg* matrix of F_A^- in any possible framework when knowing its principal *g*-values.

Step 2. The M_2 matrix being known after the attribution of numerical values to its off-diagonal elements, matrices M_1 and M_3 can be calculated from Eqs. 2 or 3. ϕ and θ angles are two more adjustable parameters involved in this step.

Step 3. The diagonal elements of M_1 and M_3 thus calculated should be as close as possible to those given in Eq. 1. The difference between the calculated (from *step 2*) and the experimental diagonal elements of M_1 and M_3 was minimized through the following indicator (**dif** being a vector and d its norm):

$$d(gg_{AB2}, gg_{AC2}, gg_{BC2}, \phi, \theta) = |\mathbf{dif}(gg_{AB2}, gg_{AC2}, gg_{BC2}, \phi, \theta)|$$

with

$$\mathbf{dif}(gg_{AB2}, gg_{AC2}, gg_{BC2}, \phi, \theta) = \begin{pmatrix} gg_{AA1}(\text{calc.}) - 3.848 \\ gg_{BB1}(\text{calc.}) - 3.646 \\ (gg_{CC1}(\text{calc.}) - 3.952)*0.5 \\ gg_{AA3}(\text{calc.}) - 4.153 \\ gg_{BB3}(\text{calc.}) - 3.731 \\ gg_{CC3}(\text{calc.}) - 3.561 \end{pmatrix}$$

The third term of **dif** contains a multiplicative factor of 0.5 because gg_{CC1} is measured with a lower precision. It can be checked that the set of Eqs. 3 is equivalent to the set of Eqs. 2 if the following transformations of parameters are used: $\theta \rightarrow \pi - \theta$; $\phi \rightarrow \phi$; $gg_{AB2} \rightarrow gg_{AB2}$; $gg_{AC2} \rightarrow -gg_{AC2}$; $gg_{BC2} \rightarrow -gg_{BC2}$. One has, therefore, $d_2(gg_{AB2}, gg_{AC2}, gg_{BC2}, \phi, \theta) = d_3(gg_{AB2}, -gg_{AC2}, -gg_{BC2}, \phi, \pi - \theta)$, d_2 and d_3 being the indicators defined above, which are calculated from sets of Eqs. 2 and 3, respectively. Moreover, it can be checked that the principal *g*-values calculated from the diagonalization of $M_2(gg_{AB2}, gg_{AC2}, gg_{BC2})$ and $M_3(gg_{AB2}, -gg_{AC2}, -gg_{BC2})$ are identical. Therefore, it is only needed to use set 2 of equations for minimizing d. This search of minima was performed by varying systematically the values of the parameters gg_{AB2}, gg_{AC2}, gg_{BC2}, ϕ, and θ. The lowest absolute minimum of d was found to correspond to adjustable parameters that are compatible with known F_A^- *g*-values, whereas other relative minima were not. A value of 0.0021 was obtained for the absolute minimum d_{min} of d, which was found for the following parameters: $gg_{AB2} = -0.034$; $gg_{AC2} = 0.114$; $gg_{BC2} = -0.122$; $\phi = 36.5°$, $\theta = 23.0°$ resulting in the following matrices:

$$M_2(d_{min}) = \begin{pmatrix} 3.521 & -0.034 & 0.114 \\ -0.034 & 4.162 & -0.122 \\ 0.114 & -0.122 & 3.760 \end{pmatrix}$$

$$M_1(\text{calc.}) = U^{-1} \times M_2 \times U = \begin{pmatrix} 3.848 & 0.108 & 0.1365 \\ 0.108 & 3.645 & 0.282 \\ 0.1365 & 0.282 & 3.950 \end{pmatrix}$$

$$M_3(\text{calc.}) = U \times M_2 \times U^{-1} = \begin{pmatrix} 4.153 & -0.099 & -0.153 \\ -0.099 & 3.730 & -0.088 \\ -0.153 & -0.088 & 3.560 \end{pmatrix}$$

the diagonal elements of which are to be compared to Eq. 1

Determination of F_A^- *g*-tensor and cocrystal parameters

Diagonalization of the M_2 matrix (or the M_1 or M_3 matrices as well) provides the principal values of the F_A^- *g*-tensor and the unitary transformation between the orthonormal frameworks (A, B, C) and (g_x, g_y, g_z): $g_x = 1.864$; $g_y = 1.9405$; $g_z = 2.050$. The three Euler angles for transforming (A, B, C) into (g_x, g_y, g_z) are 185.7°, 106.7°, and 23.3°, respectively.

REFERENCES

Adir, N., H. L. Axelrod, P. Beroza, R. A. Isaacson, S. H. Rongey, M. Y. Okamura, and G. Feher. 1996. Co-crystallization and characterization of

the photosynthetic reaction center-cytochrome c_2 complex from *Rhodobacter sphaeroides. Biochemistry.* 35:2535–2547.

Bittl, R., S. G. Zech, P. Fromme, H. T. Witt, and W. Lubitz. 1997. Pulsed EPR structure analysis of photosystem I single crystals: localization of the phylloquinone acceptor. *Biochemistry.* 36:12001–12004.

Bonnerjea, J., and M. C. W. Evans. 1982. Identification of multiple components in the intermediary electron carrier complex of photosystem I. *FEBS Lett.* 148:313–316.

Bottin, H., and B. Lagoutte. 1992. Ferredoxin and flavodoxin from the cyanobacterium *Synechocystis* sp PCC 6803. *Biochim. Biophys. Acta.* 1101:48–56.

Brettel, K. 1997. Electron transfer and arrangement of the redox cofactors in photosystem I. *Biochim. Biophys. Acta.* 1318:322–373.

Brettel, K., I. Sieckmann, P. Fromme, A. van der Est, and D. Stehlik. 1992. Low-temperature EPR on single crystals of photosystem I: study of the iron-sulfur center F_A. *Biochim. Biophys. Acta.* 1098:266–270.

Chen, L., R. C. Durley, F. S. Mathews, and V. L. Davidson. 1994. Structure of an electron transfer complex: methylamine dehydrogenase, amicyanin, and cytochrome c_{551i}. *Science.* 264:86–90.

Chen, L., R. Durley, B. J. Poliks, K. Hamada, Z. Chen, F. S. Mathews, V. L. Davidson, Y. Satow, E. Huizinga, and F. M. Vellieux. 1992. Crystal structure of an electron-transfer complex between methylamine dehydrogenase and amicyanin. *Biochemistry.* 31:4959–4964.

Fee, J. A., and G. Palmer. 1971. The properties of parsley ferredoxin and its selenium-containing homolog. *Biochim. Biophys. Acta.* 245:175–195.

Fromme, P. 1996. Structure and function of photosystem I. *Curr. Opin. Struct. Biol.* 6:473–484.

Fromme, P. 2002. Crystallization of photosystem I. *In* Methods and Results in Membrane Protein Crystallization. S. Iwata, editor. International University Line, La Jolla, Ca. in press.

Fromme, P., W. D. Schubert, and N. Krauss. 1994. Structure of photosystem I. Docking sites for plastocyanin and ferredoxin, and the coordination of P700. *Biochim. Biophys. Acta.* 1187:99–105.

Fromme, P., and H. T. Witt. 1998. Improved isolation and crystallization of photosystem I for structural analysis. *Biochim. Biophys. Acta.* 1365: 175–184.

Jordan, P., P. Fromme, H. T. Witt, O. Klukas, W. Saenger, and N. Krauss. 2001. Three-dimensional structure of cyanobacterial photosystem I at 2.5 angstrom resolution. *Nature.* 411:909–917.

Jung, Y. S., I. R. Vassiliev, F. Qiao, F. Yang, D. A. Bryant, and J. H. Golbeck. 1996. Modified ligands to F_A and F_B in photosystem I. Proposed chemical rescue to a [4Fe-4S] cluster with an external thiolate in alanine, glycine, and serine mutants of PsaC. *J. Biol. Chem.* 271: 31135–31144.

Kamlowski, A., A. van der Est, P. Fromme, and D. Stehlik. 1997. Low temperature EPR on photosystem I single crystals: orientation of the iron-sulfur centers F_A and F_B. *Biochim. Biophys. Acta.* 1319:185–198.

Kamlowski, A., S. G. Zech, P. Fromme, R. Bittl, W. Lubitz, H. T. Witt, and D. Stehlik. 1998. The radical pair state $P700^+ A_1^-$ in photosystem I single crystals: orientation dependence of the transient spin-polarized EPR spectra. *J. Phys. Chem. B.* 102:8266–8277.

Käss, P., H. Fromme, T. Witt, and W. Lubitz. 2001. Orientation and electronic structure of the primary donor radical cation $P\text{-}700^+$ in photosystem I: a single crystal EPR and ENDOR study. *J. Phys. Chem. B.* 105:1225–1239.

Knaff, D. B. 1996. Ferredoxin and ferredoxin-dependent enzymes. *In* Oxygenic Photosynthesis: The Light Reactions. D. R. Ort and C. Yocum, editors. Kluwer Academic Publishers, Dordrecht, The Netherlands. 333–361.

Krauss, N., W. Hinrichs, I. Witt, P. Fromme, W. Pritzkow, Z. Dauter, C. Betzel, K. S. Wilson, H. T. Witt, and W. Saenger. 1993. Three-dimensional structure of system I of photosynthesis at 6 Å resolution. *Nature.* 361:326–331.

Kurisu, G., M. Kusunoki, E. Katoh, T. Yamazaki, K. Teshima, Y. Onda, Y. Kimata-Ariga, and T. Hase. 2001. Structure of the electron transfer complex between ferredoxin and ferredoxin-$NADP^+$ reductase. *Nat. Struct. Biol.* 8:117–121.

Lange, C., and C. Hunte. 2002. Crystal structure of the yeast cytochrome bc_1 complex with its bound substrate cytochrome c. *Proc. Natl. Acad. Sci. U.S.A.* 99:2800–2805.

Lelong, C., E. J. Boekema, J. Kruip, H. Bottin, M. Rögner, and P. Sétif. 1996. Characterization of a redox active crosslinked complex between cyanobacterial photosystem I and soluble ferredoxin. *EMBO J.* 15: 2160–2168.

Lelong, C., P. Sétif, B. Lagoutte, and H. Bottin. 1994. Identification of the amino acids involved in the functional interaction between photosystem I and ferredoxin from *Synechocystis* sp. PCC 6803 by chemical crosslinking. *J. Biol. Chem.* 269:10034–10039.

Mathis, P., and P. Sétif. 1981. Near infra-red absorption spectra of the chlorophyll *a* cations and triplet state in vitro and in vivo. *Isr. J. Chem.* 21:316–320.

Morales, R., M. H. Charon, G. Kachalova, L. Serre, M. Medina, C. Gomez-Moreno, and M. Frey. 2000. A redox-dependent interaction between two electron-transfer partners involved in photosynthesis. *Embo Rep.* 1:271–276.

Mühlenhoff, U., J. Kruip, D. A. Bryant, M. Rögner, P. Sétif, and E. Boekema. 1996. Characterization of a redox-active cross-linked complex between cyanobacterial photosystem I and its physiological acceptor flavodoxin. *EMBO J.* 15:488–497.

Pelletier, H., and J. Kraut. 1992. Crystal structure of a complex between electron transfer partners, cytochrome c peroxidase and cytochrome c. *Science.* 258:1748–1755.

Rogers, L. J. 1987. Ferredoxins, flavodoxins and related proteins: structure, function and evolution. *In* The Cyanobacteria. P. Fay and C. Van Baalen, editors. Elsevier, Amsterdam, New York, Oxford. 35–67.

Rupp, H., A. De la Torre, and D. O. Hall. 1979. The electron spin relaxation of the electron acceptors of photosystem I reaction center studied by microwave power saturation. *Biochim. Biophys. Acta.* 548: 552–564.

Rutherford, A. W., and J. E. Mullet. 1981. Reaction center triplet states in photosystem I and photosystem II. *Biochim. Biophys. Acta.* 635: 225–235.

Sétif, P. 2001. Ferredoxin and flavodoxin reduction by photosystem I. *Biochim. Biophys. Acta.* 1507:161–179.

Sétif, P., and H. Bottin. 1994. Laser flash absorption spectroscopy study of ferredoxin reduction by photosystem I in *Synechocystis* sp. PCC 6803: evidence for submicrosecond and microsecond kinetics. *Biochemistry.* 33:8495–8504.

Sétif, P. and H. Bottin. 1995. Laser flash absorption spectroscopy study of ferredoxin reduction by photosystem I: spectral and kinetic evidence for the existence of several photosystem I-ferredoxin complexes. *Biochemistry.* 34:9059–9070.

Tagawa, K., and D. I. Arnon. 1968. Oxidation-reduction potentials and stoichiometry of electron transfer in ferredoxins. *Biochim. Biophys. Acta.* 153:602–613.

Tsukihara, T., K. Fukuyama, M. Nakamura, Y. Katsube, N. Tanaka, M. Kakudo, K. Wada, T. Hase, and H. Matsubara. 1981. X-ray analysis of a [2Fe-2S] ferredoxin from *Spirulina platensis*: main chain fold and location of side chains at 2.5 Å resolution. *J. Biochem. (Tokyo).* 90: 1763–1773.

Ullmann, G. M., M. Hauswald, A. Jensen, and E. W. Knapp. 2000. Structural alignment of ferredoxin and flavodoxin based on electrostatic potentials: implications for their interactions with photosystem I and ferredoxin-NADP reductase. *Proteins: Struct., Funct., Genet.* 38: 301–309.

Weil, J. A., J. R. Bolton, and J. E. Wertz. 1994. Electron Paramagnetic Resonance: Theory and Applications. Wiley-Interscience, New York.